Preparation of single-layer $MoS_{2x}Se_{2(1-x)}$ and $Mo_xW_{1-x}S_2$ nanosheets with high-concentration metallic 1T phase

Chaoliang Tan,[1†] Wei Zhao,[1†] Apoorva Chaturvedi,[1†] Zhen Fei,[2] Zhiyuan Zeng,[3] Junze Chen,[1] Ying Huang,[1] Peter Ercius,[4] Zhimin Luo,[1] Xiaoying Qi,[5] Bo Chen,[1] Zhuangchai Lai,[1] Bing Li,[6] Xiao Zhang,[1] Jian Yang,[1] Chuanhong Jin,[2] Haimei Zheng,[3] Christian Kloc,[1] and Hua Zhang[1]*

[1]School of Materials Science and Engineering, Nanyang Technological University, 50 Nanyang Avenue, Singapore 639798, Singapore

[2]State Key Laboratory of Silicon Materials and School of Materials Science & Engineering, Zhejiang University, Hangzhou, Zhejiang 310027, P. R. China

[3]Materials Sciences Division, Lawrence Berkeley National Laboratory, Berkeley, California 94720, United States

[4]National Center for Electron Microscopy, Molecular Foundry, Lawrence Berkeley National Lab, Berkeley, CA 94720, USA

[5]Singapore Institute of Manufacturing Technology, 71 Nanyang Drive, Singapore 638075, Singapore

[6]Institute of Materials Research and Engineering, A*STAR (Agency for Science, Technology and Research) 3 Research Link, Singapore 117602 (Singapore)

E-mail: hzhang@ntu.edu.sg. Website: http://www.ntu.edu.sg/home/hzhang/.

[†]These authors contributed equally to this work.

The ability to engineer the crystal phase of ultrathin transition metal dichalcogenide (TMD) nanosheets from semiconducting 2H phase to metallic 1T phase is of great importance for various applications. Here, we report the high-yield and scalable production of single-layer ternary TMD nanosheets with ~66% of metallic 1T phase, including $MoS_{2x}Se_{2(1-x)}$ and $Mo_xW_{1-x}S_2$, by exfoliation of their 2H-phase layered bulk crystals via our developed electrochemical Li-intercalation and exfoliation method. As a proof-of-concept application, the exfoliated single-layer $MoS_{2x}Se_{2(1-x)}$ nanosheets casted on a fluorine-doped tin oxide substrate are used as highly efficient electrocatalyst on the counter electrode for the tri-iodide reduction in a dye-sensitized solar cell. A power conversion efficiency of 6.5% is achieved, which is higher than that of 2H $MoS_{2x}Se_{2(1-x)}$ (5.4%) and MoS_2 nanosheets with ~67% of 1T phase (6.0%). The enhanced electrocatalytic activity arises from the Se doping and high-concentration metallic 1T phase of the exfoliated $MoS_{2x}Se_{2(1-x)}$ nanosheets. Our results suggest that TMD nanosheets with high-concentration 1T phase produced in high yield and large scale could be promising electrocatalysts used for highly efficient and low-cost dye-sensitized solar cells.

Keywords: Single-layer transition metal dichalcogenide nanosheets; Metallic 1T phase; $MoS_{2x}Se_{2(1-x)}$; $Mo_xW_{1-x}S_2$; Tri-iodide reduction; Dye-sensitized solar cells.

Single- and few-layer transition metal dichalcogenide (TMD) nanosheets, such as MoS_2, WS_2, $MoSe_2$, *etc.*, have attracted increasing attention in the past few years due to their unique chemical and electronic properties[1-3] as well as various promising applications in electronic/optoelectronic devices[4,5], electrocatalysis[6,7], sensors[8,9], energy storage[10,11] and biomedicine[12,13]. Ultrathin two-dimensional (2D) ternary TMD nanosheets, such as $MoS_{2x}Se_{2(1-x)}$ and $Mo_xW_{1-x}S_2$, are also receiving much attention[14-22]. The ternary structure of ultrathin 2D TMD nanosheets enables them with some appealing properties or functions, such as tunable band gaps[15-19] and enhanced catalytic activity for hydrogen generation[20,22]. Currently, single- or few-layer ternary TMD nanosheets, such as $MoS_{2x}Se_{2(1-x)}$ and $Mo_xW_{1-x}S_2$, are normally prepared by mechanical exfoliation[14,15] and chemical vapor deposition (CVD)[16-19]. However, few-layer ternary TMD flakes can be prepared by sonication-assisted exfoliation[20,21] and wet-chemical synthesis methods[22]. Therefore, it still remains a big challenge for the high-yield and large-scale preparation of single-layer ternary TMD nanosheets in solution.

Generally, ultrathin 2D TMD nanosheets have a 2H crystal phase (for example, MoS_2, WS_2 and $MoSe_2$), rendering them semiconducting properties with large band gaps of 1-2 eV and thus appealing for electronics/optoelectronics[1-3]. However, their low intrinsic electrical conductivity limited their potentials for some specific applications, such as electrodes for electrocatalysis and electrochemical supercapacitors, and low-resistance contact transistors[1-3]. Recently, it has been demonstrated that the phase engineering of ultrathin 2D TMD nanosheets from semiconducting 2H phase to metallic 1T phase is an effective approach to improve the conductivity of TMD nanosheets[23] and thus to achieve much enhanced performance in electrocatalytic hydrogen evolution[24-26], electrochemical supercapacitors[27] and low-resistance contact transistors[28,29]. Normally, the phase engineering of 2D TMD nanosheets can be achieved by the Li-intercalation

with n-butyllithium[24,25,27,28,30], laser irradiation[29], electron bean irradiation[31], and gate-controlled Li-intercalation[32]. Recently, the metallic 1T TMD nanosheets (for example, WS_2) can also be directly synthesized by the wet-chemical method[33]. Here, we use our recently developed electrochemical Li-intercalation and exfoliation method[34] to prepare the high-yield and scalable production of single-layer ternary TMD nanosheets with high-concentration metallic 1T phase (~66%), including $MoS_{2x}Se_{2(1-x)}$ and $Mo_xW_{1-x}S_2$, from their 2H-phase layered bulk crystals (Scheme 1). As a proof-of-concept application, the exfoliated $MoS_{2x}Se_{2(1-x)}$ nanosheets with high concentration of metallic 1T phase are coated on a fluorine-doped tin oxide (FTO) substrate by simple drop-coating method, which were then used as highly efficient electrocatalyst on counter electrode (CE) for the tri-iodide reduction in a dye-sensitized solar cell (DSSC).

Micrometer-sized 2H-phase layered bulk crystals of $MoS_{2x}Se_{2(1-x)}$ and $Mo_xW_{1-x}S_2$ were synthesized from their elementary powders via the chemical vapor transport method (see Method for details) (Supplementary Figure 1, 2). Based on the energy-dispersive X-ray spectroscopy (EDS) analyses (Supplementary Figure 1c, 2c), the chemical formulas of $MoS_{2x}Se_{2(1-x)}$ and $Mo_xW_{1-x}S_2$ crystals are determined to be $MoS_{1.35}Se_{0.65}$ and $Mo_{0.65}W_{0.35}S_2$, respectively. The as-prepared bulk crystals were then used as the sources to produce single-layer ternary nanosheets by using our recently developed electrochemical Li-intercalation and exfoliation method[34] (see Method for details, Scheme 1). The size and thickness of exfoliated $MoS_{2x}Se_{2(1-x)}$ nanosheet are 0.1-2 μm (Figure 1a,b,c) and 1.1-1.2 nm (Figure 1b, Supplementary Figure 3), respectively, suggesting its single-layer nature. The obtained $MoS_{2x}Se_{2(1-x)}$ nanosheet can be well-dispersed in water to form a stable colloidal suspension (inset in Figure 1a). The selected area electron diffraction (SAED) pattern of a typical $MoS_{2x}Se_{2(1-x)}$ nanosheet (Figure 1d) shows bright diffraction spots with six-fold symmetry (Figure 1e). The outer and inner six spots can be

indexed to the (110) and (100) planes of $MoS_{2x}Se_{2(1-x)}$, respectively. The high-resolution TEM (HRTEM) image gives continuous lattice fringes with lattice distance of 0.276 nm (Figure 1f), assignable to the (100) planes of $MoS_{2x}Se_{2(1-x)}$ crystal. The signals of Mo, S and Se can be observed in its EDS spectrum (Supplementary Figure 4) and their homogeneous distribution in the nanosheet is clearly evidenced by the elemental mapping (Figure 1g).

The S and Se atoms in the $MoS_{2x}Se_{2(1-x)}$ nanosheet can be observed in the high-angle annual dark-field (HAADF) image obtained by using an aberration-corrected scanning transmission electron microscope (STEM). Figure 2a clearly shows the triangular arrangement of Mo atoms, indicating the 1T phase structure of $MoS_{2x}Se_{2(1-x)}$ nanosheet. Since the atom image intensity is directly related to the Z number of the atoms, the Se atom gives a brighter contrast than does the S atom due to its larger Z number[16]. The STEM image of $MoS_{2x}Se_{2(1-x)}$ nanosheet shows that the Se atoms randomly occupied the S sites in the single-layer ternary nanosheet, while the S atoms cannot be distinguished because they show negligible contrast in the STEM image of 1T-phase $MoS_{2x}Se_{2(1-x)}$ due to the smaller Z number of S atom (Figure 2a, Supplementary Figure 5).

Furthermore, the presence of high-concentration metallic 1T crystal phase in the exfoliated $MoS_{2x}Se_{2(1-x)}$ nanosheets was confirmed by X-ray photoelectron spectroscopy (XPS), Raman spectroscopy and UV-vis absorption spectroscopy. In order to quantitatively calculate the concentration of 1T phase, XPS was used to study the phase compositions in the bulk crystal of $MoS_{2x}Se_{2(1-x)}$, and the exfoliated nanosheets of $MoS_{2x}Se_{2(1-x)}$ before and after annealing at 300℃ under Ar (Figure 2b, Supplementary Figure 6). The Mo 3d spectrum of bulk crystal gives peaks at around 229.0 and 232.1 eV (Figure 2b), assignable to Mo^{4+} $3d_{5/2}$ and Mo^{4+} $3d_{3/2}$ of 2H-phase $MoS_{2x}Se_{2(1-x)}$, respectively[35,36]. The deconvolution of Mo 3d spectrum of exfoliated nanosheets indicates that the two main peaks shifted to lower binding energy by ~0.8 eV (228.2 and 231.3

eV, red peaks) with respect to the position of 2H $MoS_{2x}Se_{2(1-x)}$ peaks (229.0 and 232.1 eV) (Figure 2b). Moreover, the additional peaks at 161.2 and 162.4 eV (or 53.5 and 54.5 eV) (red peaks) appeared besides the known peaks of 2H phase $MoS_{2x}Se_{2(1-x)}$ at 161.9 and 163.1 eV (or 54.2 and 55.2 eV) (olive peaks) in the S 2p (or Se 2d) spectra (Supplementary Figure 6)[36,37]. All the analyses of XPS Mo 3d, S 2p and Se 2d spectra prove the presence of 1T phase in the exfoliated $MoS_{2x}Se_{2(1-x)}$ nanosheets, which is similar to that of chemically exfoliated 1T MoS_2 nanosheets[30]. The calculated concentration of 1T phase is as high as ~66% based on the Mo 3d spectrum (Figure 2b). Note that the 1T peaks can be totally quenched after the exfoliated $MoS_{2x}Se_{2(1-x)}$ nansoheets were annealed at 300℃ (Figure 2b, Supplementary Figure 6), suggesting the restoration of 2H phase from 1T phase[24,30]. Raman spectroscopy was used to characterize the aforementioned three $MoS_{2x}Se_{2(1-x)}$ samples. Three prominent peaks corresponding to the 2H MoS_2-like A_{1g} (402 cm^{-1}) and E^1_{2g} (374 cm^{-1}) modes and the 2H $MoSe_2$-like E^1_{2g} (272 cm^{-1}) mode are clearly observed in three samples (Figure 2c)[37]. Only the exfoliated $MoS_{2x}Se_{2(1-x)}$ nanosheet exhibits small peaks, around 140 and 300 cm^{-1}, in the lower frequency region (Figure 2c), corresponding to the distorted 1T phase Raman active modes, J_1 and J_3, respectively, which are similar to the chemically exfoliated 1T MoS_2 nansoheets[30]. The presence of 1T phase in exfoliated $MoS_{2x}Se_{2(1-x)}$ nanosheets was also evidenced by the absorption spectra (Figure 2d). No obvious characteristic peaks of 2H $MoS_{2x}Se_{2(1-x)}$ can be observed in the exfoliated $MoS_{2x}Se_{2(1-x)}$ nanosheet film, except a small peak at around 380 nm (Figure 2d). In contrast, after annealing of the exfoliated $MoS_{2x}Se_{2(1-x)}$ film at 300℃, the characteristic A and B excitonic peaks of 2H $MoS_{2x}Se_{2(1-x)}$ at 650 and 715 nm, respectively, and the convoluted C and D excitonic peaks at around 443 nm were clearly observed (olive curve in Figure 2d), suggesting the restoration of 2H phase[30].

Similarly, the single-layer ternary $Mo_xW_{1-x}S_2$ nanosheets with high-concentration metallic 1T phase can also be prepared by exfoliation of its bulk crystal using the same method (Figure 3), and the stable colloidal suspension of $Mo_xW_{1-x}S_2$ nanosheets was obtained (inset in Figure 3a)[34]. The well-dispersed $Mo_xW_{1-x}S_2$ nanosheets with size similar to $MoS_{2x}Se_{2(1-x)}$ nanosheets were confirmed by the SEM, AFM and low-magnification TEM images (Figure 3a,b,c). The typical thickness of $Mo_xW_{1-x}S_2$ nanosheets is 0.9-1.2 nm (Figure 3b, Supplementary Figure 7), proving their single-layer nature. The hexagonal diffraction spots can be observed from the SAED pattern of a typical $Mo_xW_{1-x}S_2$ nanosheet (Figure 3d,e). The outside and inner six spots the SAED pattern are corresponding to the (110) and (100) planes of the $Mo_xW_{1-x}S_2$ nanosheet, respectively. The HRTEM image reveals the continuous lattice fringe with a lattice spacing of ~0.272 nm (Figure 3f), assignable to the (100) planes of the $Mo_xW_{1-x}S_2$ crystal. The EDS spectrum of a typical $Mo_xW_{1-x}S_2$ nanosheet gives strong signals of Mo, W and S (Supplementary Figure 8) and these elements are homogeneously distributed in the ternary nanosheet (Supplementary Figure 9).

Moreover, the STEM was used to visualize the distribution of Mo and W atoms in the single-layer $Mo_xW_{1-x}S_2$ nanosheet. The atomic STEM image shows that the W and Mo atoms are randomly distributed in the single-layer nanosheet, forming a hexagonal lattice arrangement. Due to the greater Z number of W atom, it shows brighter contrast than does the Mo atoms. (Supplementary Figure 10). In addition, the XPS analyses of three $Mo_xW_{1-x}S_2$ samples give similar results with the three $MoS_{2x}Se_{2(1-x)}$ samples, respectively. The exfoliated $Mo_xW_{1-x}S_2$ nanosheets show obvious shift to lower binding energy in comparison with the 2H bulk crystal in the Mo 3d, S 2p and W 4f spectra, and the quenching of the 1T phase peaks can be observed after annealing (Figure 3g,h, Supplementary Figure 11). The calculated concentration of metallic 1T phase is also as high as ~66% for the exfoliated $Mo_xW_{1-x}S_2$ based on the Mo 3d spectrum

(Figure 3g). Similarly, all the three $Mo_xW_{1-x}S_2$ samples show three prominent peaks at 407, 380 and 357 cm^{-1} (Figure 3i), corresponding to the MoS_2-like A_{1g}, E^1_{2g} and WS_2-like E^1_{2g} modes of 2H $Mo_xW_{1-x}S_2$, respectively[38]. The distorted 1T phase Raman active modes (J_1: 150 cm^{-1}, and J_2: 215 cm^{-1}) in the lower frequency region can be observed in the exfoliated $Mo_xW_{1-x}S_2$ nanosheets (Figure 3i)[30]. The UV-vis absorption spectra give similar results to the $MoS_{2x}Se_{2(1-x)}$ nanosheet films, revealing the metallic 1T phase in the exfoliated $Mo_xW_{1-x}S_2$ nanosheets and the restoration of 2H phase after the exfoliated $Mo_xW_{1-x}S_2$ nanosheets were annealed at 300℃ (Supplementary Figure 12).

As known, the single-layer MoS_2 nanosheets with high concentration of metallic 1T phase were prepared by exfoliating its bulk crystal via our Li-intercalation and exfoliation method.[34] The detail characterizations of bulk crystal of MoS_2, and exfoliated and annealed MoS_2 nanosheets by SEM, AFM, TEM, XPS, Raman spectroscopy and UV-vis spectroscopy are shown in Supplementary Figure 13-17. All these results indicate that the exfoliated MoS_2 nanosheets also contain a high concentration of metallic 1T phase (~67%) (Supplementary Figure 15a). It proved the coexistence of 2H and 1T phases in the single-layer MoS_2 nanosheets[39]. In this study, we have successfully used our electrochemical Li-intercalation and exfoliation method to prepare single-layer ternary TMD nanosheets with high concentration of metallic 1T phase with the layered 2H-phase bulk crystals as the source. The phase transformation from semiconducting 2H phase to metallic 1T phase occurs during the electrochemical Li-intercalation. Alternatively, in the previously reported intercalation of TMD bulk materials with n-butyllithium[23,30], during the intercalation process, it is believed that the electron transfer from the butyl to TMDs occurs, which destabilizes the pristine 2H phase and thus to induce the phase transformation from 2H phase to metallic 1T phase[23,30]. However, in our study, the electrons should be donated from the

Li foil to TMD crystals (i.e., MoS_2, $MoS_{2x}Se_{2(1-x)}$ and $Mo_xW_{1-x}S_2$) during the discharge process (Scheme 1)[40,41], thus leading to the phase transformation to obtain TMD nanosheets with high-concentration metallic 1T phase. We believe that our method can also be used to effectively exfoliate other TMD materials and induce the phase transformation in the obtained single- or few-layer TMD nanosheets.

As known, TMD nanomaterials, such as MoS_2 and WS_2 particles[42] and few-layer $MoSe_2$ nanosheets[43], can be used as cost-effective electrocatalysts in the CEs of DSSCs, which show good photovoltaic performance. Here, as a proof-of-concept application, single-layer $MoS_{2x}Se_{2(1-x)}$ nanosheets with ~66% of metallic 1T phase were used as electrocatalysts for the tri-iodide reduction in I^-/I_3^- redox electrolyte in DSSCs, which exhibit higher electrocatalytic activity compared to the 2H-phase single-layer $MoS_{2x}Se_{2(1-x)}$ nanosheets and the single-layer MoS_2 nanosheets with ~67% of metallic 1T phase. In a typical experiment, the exfoliated single-layer $MoS_{2x}Se_{2(1-x)}$ nanosheet coated on a FTO substrate, referred to as FTO-Exfoliated-$MoS_{2x}Se_{2(1-x)}$, by simple drop-casting method was used as the CE in a DSSC, in which an N719 dye-sensitized mesoporous TiO_2 electrode was used as the photoanode[44]. The schematic illustration of DSSC device is shown in Figure 4a. The deposited $MoS_{2x}Se_{2(1-x)}$ nanosheet film has a thickness of ~50 nm (Supplementary Figure 18). The 2H-phase $MoS_{2x}Se_{2(1-x)}$ nanosheet film on FTO, referred to as FTO-Annealed-$MoS_{2x}Se_{2(1-x)}$, was obtained by annealing the FTO-Exfoliated-$MoS_{2x}Se_{2(1-x)}$ under Ar atmosphere at 300℃ for 1 h. Figure 4b illustrates the photocurrent density-voltage (*J*-*V*) characteristic curves of DSSCs with three different CEs. The detailed photovoltaic parameters are summarized in Table 1. In a control experiment, the DSSC using the Pt-decorated FTO, referred to as FTO-Pt, as CE has an open-circuit voltage (V_{oc}) of 0.80 V, a short-circuit current density (J_{sc}) of 12.82 mA cm^{-2}, a fill factor (*FF*) of 0.69, and a PCE of 7.0%. When the FTO-

Exfoliated-$MoS_{2x}Se_{2(1-x)}$ was used as CE, the photovoltaic parameters, V_{oc}, J_{sc}, *FF* and PCE are 0.75 V, 13.40 mA cm^{-2}, 0.65, and 6.5%, respectively. Although the FTO-Pt CE exhibits a little higher V_{oc} and *FF*, the FTO-Exfoliated-$MoS_{2x}Se_{2(1-x)}$ gives a little higher J_{sc}. Therefore, their photovoltaic performance is comparable. In contrast, when the FTO-Annealed-$MoS_{2x}Se_{2(1-x)}$ was used as CE, the PCE is only 5.4% with V_{oc}=0.76 V, J_{sc}=13.52 mA cm^{-2}, and FF=0.52. Although the changes of V_{oc} and J_{sc} are quite small, its FF shows a notable decrease compared to the other two CEs. For comparison, the photovoltaic performance of exfoliated MoS_2 nanosheets with ~67% of metallic 1T phase and annealed MoS_2 nanosheets with 2H phase deposited on FTO electrodes, referred to as FTO-Exfoliated-MoS_2 and FTO-Annealed-MoS_2, respectively, were also measured. Similarly, the FTO-Exfoliated-MoS_2 also gives a higher FF (0.65) and PEC (6.0%) compared to the FTO-Annealed-MoS_2 (FF=0.58 and PCE=5.1%) (Supplementary Figure 19, Supplementary Table 1). Based on the aforementioned results, both of the exfoliated $MoS_{2x}Se_{2(1-x)}$ and MoS_2 nanosheets with high concentration of 1T phase display better photovoltaic performance compared to the 2H ones after annealing.

The higher photovoltaic performance of exfoliated $MoS_{2x}Se_{2(1-x)}$ should be ascribed to its higher electrocatalytic activity towards the tri-iodide reduction in comparison with the annealed one, which is supported by the cyclic voltammetry (CV) and electrochemical impedance spectroscopy (EIS). The CV curves in Figure 4c give two typical pairs of redox peaks for both FTO-Exfoliated-$MoS_{2x}Se_{2(1-x)}$ and FTO-Pt CEs, indicating the Pt-like electrocatalytic activity of exfoliated $MoS_{2x}Se_{2(1-x)}$ nanosheets in the tri-iodide reduction. The two peaks correspond to the two-step reversible redox reaction in the I^-/ I_3^- electrolyte solution, i.e. the left pair (Ox-1 and Red-1): $I_3^- + 2e^- \leftrightarrow 3I^-$, and the right pair (Ox-2 and Red-2): $3I_2 + 2e^- \leftrightarrow 2I_3^-$. However, one of the anodic peaks (Ox-2) could not be observed in the FTO-Annealed-$MoS_{2x}Se_{2(1-x)}$ CE. Moreover,

the cathodic peak density of Red-1 in FTO-Exfoliated-$MoS_{2x}Se_{2(1-x)}$ is higher than that of the FTO-Annealed-$MoS_{2x}Se_{2(1-x)}$, suggesting a faster redox reaction on FTO-Exfoliated-$MoS_{2x}Se_{2(1-x)}$ CE[45]. Therefore, from the CV analysis, the FTO-Exfoliated-$MoS_{2x}Se_{2(1-x)}$ CE exhibits better electrocatalytic activity compared to FTO-Annealed-$MoS_{2x}Se_{2(1-x)}$ CE. Similarly, the CV curves of FTO-Exfoliated-MoS_2 and FTO-Annealed-MoS_2 CEs were also obtained and compared in Supplementary Figure 19a, further demonstrating the higher electrocatalytic activity of the exfoliated nanosheets compared to the one after annealing.

Furthermore, the electron transport process at the CE/electrolyte interface was studied by the EIS measurement in a symmetric dummy cell consisting of two identical CEs. Figure 4d shows the Nyquist plots for the $MoS_{2x}Se_{2(1-x)}$ samples obtained in the dark without bias potential, which are fitted with the equivalent circuit (inset in Figure 4d)[46]. The semicircle in the high frequency region presents the charge transfer resistance (R_{ct}) and the corresponding constant phase angle element (CPE) at the CE/electrolyte interface. The arch in the low frequency region indicates the diffusion resistance (Z_N) of the redox couple in the electrolyte. The intercept on the real axis is defined as the ohmic series resistance (R_s). In these parameters, R_{ct} and R_s are highly related to the electrocatalytic activity of CEs for the tri-iodide reduction. The obtained R_{ct} and R_s for two $MoS_{2x}Se_{2(1-x)}$ CEs are summarized in Table 1. Obviously, the FTO-Annealed-$MoS_{2x}Se_{2(1-x)}$ has a slightly lower R_s (27.92 Ω cm^2) compared to the FTO-Exfoliated-$MoS_{2x}Se_{2(1-x)}$ (28.40 Ω cm^2), which might arise from the enhanced adhesion between the electrocatalyst layer (i.e. $MoS_{2x}Se_{2(1-x)}$ film) and FTO substrate after the thermal annealing[46]. However, compared to FTO-Annealed-$MoS_{2x}Se_{2(1-x)}$ with R_{ct} of 23.25 Ω cm^2, the FTO-Exfoliated-$MoS_{2x}Se_{2(1-x)}$ gives much lower R_{ct} (4.60 Ω cm^2), close to that of FTO-Pt CE (2.28 Ω cm^2), suggesting its higher electrocatalytic activity. Based on the previous report on the equivalent circuit model for DSSCs[47], the FF is

inversely proportional to the sum of R_s and R_{ct}. Due to the small difference of R_s for FTO-Exfoliated-$MoS_{2x}Se_{2(1-x)}$ and FTO-Annealed-$MoS_{2x}Se_{2(1-x)}$, the higher R_{ct} (23.25 Ω cm^2) contributes to the lower FF of FTO-Annealed-$MoS_{2x}Se_{2(1-x)}$. As known, the higher R_{ct} may be ascribed to the lower conductivity of the semiconducting 2H-phase $MoS_{2x}Se_{2(1-x)}$ after annealing of the exfoliated-$MoS_{2x}Se_{2(1-x)}$[25], which induces the sluggish electron transfer process. In contrast, the high concentration of metallic 1T phase in the FTO-Exfoliated-$MoS_{2x}Se_{2(1-x)}$ (~66%) renders its higher conductivity, which can facilitate the electron transport from the CE surface to the redox electrolyte for the tri-iodide reduction. Similarly, the FTO-Exfoliated-MoS_2 also gives a higher FF (0.65) because of its much lower R_{ct} (19.60 Ω cm^2) compared to the FTO-Annealed-MoS_2 (FF=0.58 and R_{ct}=121.1 Ω cm^2) (Supplementary Figure 20a and Supplementary Table 1), indicating the higher electrocatalytic activity of the exfoliated MoS_2 nanosheets compared to those after annealing. Impressively, the FTO-Exfoliated-$MoS_{2x}Se_{2(1-x)}$ gives R_{ct} of 4.60 Ω cm^2, much lower than that of the FTO-Exfoliated-MoS_2 with R_{ct} of 19.60 Ω cm^2 (Supplementary Figure 20b). The much lower R_{ct} of exfoliated $MoS_{2x}Se_{2(1-x)}$ compared to the exfoliated MoS_2 with similar concentration of 1T phase can be ascribed to higher conductivity induced by Se doping (Supplementary Figure 20b)[48], resulting in its higher catalytic activity towards the tri-iodide reduction. Therefore, when integrated in a DSSC device, the FTO-Exfoliated-$MoS_{2x}Se_{2(1-x)}$ gives a higher PEC (6.5%) than does FTO-Exfoliated-MoS_2 (6.0%).

Based on all the aforementioned discussion, we uncover that the FTO-Exfoliated-$MoS_{2x}Se_{2(1-x)}$ gives higher electrocatalytic activity towards the tri-iodide reduction compared to the FTO-Exfoliated-MoS_2 and FTO-Annealed-$MoS_{2x}Se_{2(1-x)}$. Therefore, when used as a CE in DSSC and compared to other nanosheets investigated in this study, the FTO-Exfoliated-$MoS_{2x}Se_{2(1-x)}$ exhibits the best photovoltaic performance (PCE=6.5%), little lower than that of FTO-Pt

(PCE=7.0%). Considering the high-performance device is incorporated with the nanosheet film deposited by simple drop-casting method at room temperature, the as-prepared nanosheets can be coated on flexible substrates to construct flexible photovoltaic devices in the near future.

In summary, single-layer ternary TMD nanosheets with high concentration of metallic 1T phase, including $MoS_{2x}Se_{2(1-x)}$ and $Mo_xW_{1-x}S_2$, have been prepared in high yield and large amount from their 2H-phase layered bulk crystals via our recently developed electrochemical Li-intercalation and exfoliation method. To the best of our knowledge, it is the first time to realize the preparation of single-layer ternary TMD nanosheets with high concentration of metallic 1T phase (~66%) at high yield and large scale. The exfoliated ternary $MoS_{2x}Se_{2(1-x)}$ nanosheets can be easily coated on a FTO by simple drop-coating method, and then directly used as highly efficient electrocatalyst for the tri-iodide reduction on the CE in a DSSC. It showed a PCE of 6.5%, which is higher than that of the annealed $MoS_{2x}Se_{2(1-x)}$ (5.4%) and exfoliated MoS_2 (6.0%). The facile, highly efficient, scalable production of single-layer $MoS_{2x}Se_{2(1-x)}$ nanosheets with high concentration of metallic 1T phase make it a promising electrocatalyst for fabrication of high-performance Pt-free DSSCs. Moreover, this nanosheet could also be promising for other applications including the electrocatalytic hydrogen evolution, supercapacitors and electrochemical sensors.

Method

Chemicals. Molybdenum powder (~22 mesh, 99.9975%, Puratronic®), sulfur pieces (99.999%, Puratronic®), tungsten powder (~22 mesh, 99.999%, Puratronic®) and selenium shots (1-3 mm, 99.999%, Puratronic®) were purchased from Alfa Aesar. Poly (vinylidene fluoride) (PVDF), acetone and N-methylpyrrolidone (NMP) were purchased from Sigma (Germany). Molybdenum

disulfide (MoS_2) bulk crystal with size of 10-30 mm was purchased from Rose Mill (USA). Lithium-ion battery electrolyte, i.e. 1M of $LiPF_6$ dissolved in a mixture of ethyl carbonate (EC) and dimethyl carbonate (DMC) (1:1 in volume ratio), was purchased from Charslton Technologies Pte Ltd. (Singapore). Lithium and copper foils were purchased from ACME Research Support Pte Ltd (Singapore). N719 dye and TiO_2 paste (18NR-T paste and WER2-O paste) were purchased from Dyesol (Australia). All the chemicals were used as received without further purification. The Milli-Q water (Milli-Q System, Millipore) was used in all experiments.

Preparation of ternary $MoS_{2x}Se_{2(1-x)}$ and $Mo_xW_{1-x}S_2$ bulk crystals. The chemical vapor transport (CVT) reaction technique was used to prepare micrometer-sized layered bulk crystals of ternary $MoS_{2x}Se_{2(1-x)}$ and $Mo_xW_{1-x}S_2$ from their elementary powders[49]. Stoichiometric amounts of Mo, S and Se (or Mo, W and S), i.e. 490.0 mg Mo, 252.0 mg S and 258.0 mg Se (or 320.4 mg Mo, 304.0 mg W and 375.6 mg S) in the total weight of 1 g, were sealed in quartz ampoule with an internal pressure in the range of 10^{-5} to 10^{-6} torr. In addition, 40 mg of iodine were also incorporated in the tube as the transport agent. The sealed tube was then put into a two-zone horizontal tube furnace (Supplementary Scheme 1). Initially, the source zone (Zone I) was kept at 800 °C and the growth zone (Zone II) was kept at 950 °C for 48 h. After that, the temperature of Zone I was gradually increased to 1030 °C at increasing rate of 10 °C/min, while the growth zone was kept at 950 °C. The reaction was kept for 120 h. Finally, both of two zones were naturally cooled down to room temperature. The final product, i.e. $MoS_{2x}Se_{2(1-x)}$ (or $Mo_xW_{1-x}S_2$) bulk crystal, was taken out from the tube for further characterization and exfoliation. The chemical formulas of the prepared $MoS_{2x}Se_{2(1-x)}$ and $Mo_xW_{1-x}S_2$ bulk crystals estimated by EDS are $MoS_{1.35}Se_{0.65}$ (Supplementary Figure 1) and $Mo_{0.65}W_{0.35}S_2$ (Supplementary Figure 2), respectively.

Preparation of single-layer ternary $MoS_{2x}Se_{2(1-x)}$ and $Mo_xW_{1-x}S_2$ nanosheets with high-concentration metallic 1T phase. By using the electrochemical Li-intercalation and exfoliation method, which was developed by our group for production of single-layer transition metal dichachogenide nanosheets[34], single-layer ternary $MoS_{2x}Se_{2(1-x)}$ and $Mo_xW_{1-x}S_2$ nanosheets with high concentration of metallic 1T phase were prepared. In a typical experiment, the powder of layered $MoS_{2x}Se_{2(1-x)}$ or $Mo_xW_{1-x}S_2$ crystal was mixed with acetylene black and PVDF binder dispersed in NMP with the mass ratio of 8:1:1. The homogeneously mixed slurry was then uniformly coated onto a copper foil disc. The as-prepared electrode was first dried in air and then dried overnight under vacuum at 100°C. The battery cell was assembled in an Ar-filled glove box. The lithium intercalation of as-prepared cathode electrode coated with $MoS_{2x}Se_{2(1-x)}$ or $Mo_xW_{1-x}S_2$ crystal was performed in a test cell using the Li foil as anode and 1M $LiPF_6$ as electrolyte. The electrochemical Li-intercalation (galvanostatic discharge) of the electrode was conducted in a Neware battery test system. After the discharge process, the electrode was taken out from the battery cell and washed with acetone to remove any residual electrolyte ($LiPF_6$), followed by sonication in water. After the suspension was centrifuged and washed with water, the final product, i.e. single-layer ternary $MoS_{2x}Se_{2(1-x)}$ or $Mo_xW_{1-x}S_2$ nanosheets, was collected for further characterization. The single-layer MoS_2 nanosheets with high concentration of metallic 1T phase were also prepared by the same method with the commercial bulk MoS_2 crystal as precursor.

Characterization. A drop of a solution containing the exfoliated TMD nanosheets was placed on a holey carbon-coated copper grid and Si or SiO_2/Si substrate, and then naturally dried in air prior to characterization. The exfoliated TMD nanosheets were drop-casted onto glass substrates to form homogenous thin films for UV-vis measurement. During the annealing process, all the

samples deposited on specific substrates (glass, Si or FTO) were annealed at 300°C for 1 h under Ar atmosphere prior to further characterization and experiments. A transmission electron microscope (JEOL JEM-2100F) coupled with energy dispersive X-ray spectroscopy (EDS) was used to record the transmission electron microscopy (TEM) images, EDS spectra and elemental mappings. The annular dark-field scanning transmission electron microscope (ADF-STEM) images were recorded on a probe-corrected Titan ChemiSTEM (FEI, USA) at an acceleration voltage of 200 kV. In order to get better contrast, the atomic images were acquired through superposition of a slice of drift corrected images. Tapping mode atomic force microscope (AFM) images were obtained on a Dimension 3100 AFM with Nanoscope IIIa controller (Veeco, CA, USA) under ambient conditions. A Bruker D8 diffractometer (German) with a Cu Kα (λ=1.54178 Å) X-ray source was used to measure the powder X-ray diffraction (XRD) patterns. X-Ray photoelectron spectroscopy (XPS) measurements were conducted using VG ESCALAB 220i-XL instrument (base pressure$<5\times10^{-10}$ mbar) equipped with a monochromatic Al Kα (1486.7 eV) X-ray source. The carbon 1 s peak located at 284.5 eV was used as the reference to calibrate all of the XPS spectra. The concentration of metallic 1T phase in the exfoliated nanosheets is calculated based on the integral areas of 2H and 1T phases after the deconvolution of their Mo 3d peaks.[30,41] A WITec CRM200 confocal Raman microscopy system with the excitation line of 532 nm and air cooling charge coupled device as the detector (WITec Instruments Corp, Germany) was used to measure the Raman spectra. The Raman band of a silicon wafer at 520 cm^{-1} was used as the reference to calibrate the spectrometer. UV-vis absorption spectra were recorded on a Shimadzu UV-1800 UV-vis spectrophotometer.

Fabrication and performance measurement of dye-sensitized solar cells (DSSCs). The TiO_2 photoanode was fabricated by the screen printing method described elsewhere[50]. The TiO_2

photoanode consists of three layers, i.e. blocking layer, transparent layer and scattering layer. First, the commercial FTO substrate (2.2 mm thickness, 15 Ω/sq, Latech) was cleaned by subsequent sonication in 15 mL of acetone, 15 mL of distilled water, and then 15 mL of ethanol for 10 min each. The blocking layer with thickness of about 50 nm was obtained by soaking the cleaned FTO substrate in a 40 mM aqueous $TiCl_4$ solution at 70 °C for 30 min, which was rinsed with water and ethanol. The transparent TiO_2 layer (Dyesol, 18NR-T paste) with thickness of about 10 μm was deposited by screen printing method (mesh count is 90 T/cm, deposition areas are 0.196 cm^2) on the blocking layer coated FTO substrate. After drying at 125 °C for 6 min, the scattering TiO_2 layer (Dyesol, WER2-O paste) with thickness of about 4 μm was superimposed by screen-printing method. The as-deposited TiO_2 photoanode was gradually annealed under air at 125°C for 10 min, 325°C for 5 min, 375°C for 5 min, 450°C for 15 min, and finally 500°C for 15 min. After the annealing temperature decreased to about 80°C, the TiO_2 photoanode was immersed into 0.3 mM of ruthenium dye N719 solution in a mixture of acetonitrile and tert-butyl alcohol (volume ratio, 1:1) at room temperature for 24 h.

Pt sputtered on FTO (FTO-Pt), the exfoliated $MoS_{2x}Se_{2(1-x)}$ nanosheet film coated on FTO (FTO-Exfoliated-$MoS_{2x}Se_{2(1-x)}$) or MoS_2 nanosheet film coated on FTO (FTO-Exfoliated-MoS_2) was used as a counter electrode (CE). The TMD nanosheet films were deposited by drop casting method on FTO substrates with a confined area about 1 cm^2 by mask. The concentration of the TMD nanosheet suspension was ~0.5 mg mL^{-1}. 100 μL of the TMD suspension was drop-casted on the confined area and then dried at room temperature overnight. Then, the FTO-Exfoliated-$MoS_{2x}Se_{2(1-x)}$ or FTO-Exfoliated-MoS_2 electrode was annealed at 300°C for 1 h under Ar atmosphere to obtain the FTO-Annealed-$MoS_{2x}Se_{2(1-x)}$ or FTO-Annealed-MoS_2 electrode, respectively, which was then used as CE. The electrolyte is a mixture containing 0.1 M of

lithium iodide (LiI), 0.6 M of tetrabutylammonium iodide (TBAI), 0.05 M of iodine (I_2), and 0.5 M of 4-tert-butylpyridine dissolved in acetonitrile. The photoanode and CE were assembled into a sandwich-type cell, which was separated by a piece of parafilm as spacer to prevent the short circuit. The active area of solar cell devices is 0.138 cm^2, which is confined by a circular mask.

Photocurrent density-voltage (*J-V*) characteristics were measured using a Keithley Model 2440 source meter under AM 1.5 illumination. A 1000 W Oriel solar simulator used as a light source was calibrated to one sun light intensity by using a NREL-calibrated Si cell (Oriel 91150). Cyclic voltammetry (CV) was performed with a CHI760D electrochemical workstation in a three-electrode setup, consisting of the FTO-Pt, FTO-Exfoliated-$MoS_{2x}Se_{2(1-x)}$, FTO-Annealed-$MoS_{2x}Se_{2(1-x)}$, FTO-Exfoliated-MoS_2, or FTO-Annealed-MoS_2, as working electrode, a platinum wire as counter electrode, and a Ag/AgCl as reference electrode. The scan rate is 50 mV s^{-1}. The electrochemical impedance spectroscopy (EIS) measurements were conducted in the dark with a computer-controlled potentiostat (Solartron1287, UK) by applying an AC voltage with 10 mV amplitude in the frequency range from 0.1 Hz to 100 kHz. The symmetrical cell with an effective area of 1 cm^2 for the recording EIS spectra was assembled with two identical CEs. The obtained EIS spectra were fitted by the Zview software to obtain the EIS parameters.

Acknowledgments

This work was supported by MOE under AcRF Tier 2 (ARC 26/13, No. MOE2013-T2-1-034; ARC 19/15, No. MOE2014-T2-2-093) and AcRF Tier 1 (RGT18/13, RG5/13), and NTU under Start-Up Grant (M4081296.070.500000) in Singapore. This Research is also conducted by NTU-HUJ-BGU Nanomaterials for Energy and Water Management Programme under the Campus for Research Excellence and Technological Enterprise (CREATE), that is supported by the National Research Foundation, Prime Minister's Office, Singapore. Z.F. and C.J. acknowledged the

Center of Electron Microscopy of Zhejiang University for the access to the probe-corrected STEM, and the financial support by the MOST (2014CB932500, 2015CB921000), the NSFC (51222202 and 51472215).

Author contributions

H.Z. proposed the research direction and guided the project. C.T. designed and performed the synthesis and characterization of single-layer $MoS_{2x}Se_{2(1-x)}$ and $Mo_xW_{1-x}S_2$ nanosheets. W.Z. fabricated DSSC devices and conducted the electrochemical measurements. A.C. and C.K. synthesized the bulk crystals of $MoS_{2x}Se_{2(1-x)}$ and $Mo_xW_{1-x}S_2$. C.T., W.Z., A.C. and H.Z. analysed and discussed the experimental results, and drafted the manuscript. Z.F. and C.J. performed STEM characterization. Z.Z., J.C., Y.H., P.E., Z.L., X.Q., B.C., Z.L., B.L., X.Z., J.Y. and H.Z (Haimei Zheng) performed some supporting experiments. All authors contributed to the manuscript.

Additional information

Supplementary information is available in the online version of the paper. Reprints and permissions information is available online at www.nature.com/reprints. Correspondence and requests for materials should be addressed to H.Z.

Competing financial interests: The authors declare no competing financial interests.

References

1. Wang, Q. H., Kalantar-Zadeh, K., Kis, A., Coleman, J. N. & Strano, M. S. Electronics and optoelectronics of two-dimensional transition metal dichalcogenides. *Nat. Nanotechnol*. **11**, 699-712 (2012).
2. Chhowalla, M. *et al.* The chemistry of two-dimensional layered transition metal dichalcogenide nanosheets. *Nat. Chem.* **5**, 263-275 (2013).
3. Huang, X., Zeng, Z. Y. & Zhang, H. Metal dichalcogenide nanosheets: preparation, properties and applications. *Chem. Soc. Rev.* **42**, 1934-1946 (2013).
4. Radisavljevic, B., Radenovic, A., Brivio, J., Giacometti, V. & Kis, A. Single-layer MoS_2 transistors. *Nat. Nanotechnol.* **6**, 147-150 (2011).
5. Yin, Z. Y. *et al.* Single-layer MoS_2 phototransistors. *ACS Nano* **6**, 74-80 (2012).
6. Xie, J. F. *et al.* Controllable disorder engineering in oxygen-incorporated MoS_2 ultrathin nanosheets for efficient hydrogen evolution. *J. Am. Chem. Soc.* **135**, 17881-17888 (2013).
7. Cheng, L. *et al.* Ultrathin WS_2 nanoflakes as a high-performance electrocatalyst for the hydrogen evolution reaction. *Angew. Chem. Int. Ed.* **53**, 7860-7863 (2014).
8. Zhu, C. F. *et al.* Single-layer MoS_2-based nanoprobes for homogeneous detection of biomolecules. *J. Am. Chem. Soc.* **135**, 5998-6001 (2013).
9. Perkins, F. K. *et al.* Chemical vapor sensing with monolayer MoS_2. *Nano Lett.* **13**, 668-673 (2013).
10. Sun, Y. F., Gao, S. & Xie, Y. Atomically-thick two-dimensional crystals: electronic structure regulation and energy device construction. *Chem. Soc. Rev.* **43**, 530-546 (2014).
11. Du, G. *et al.* Superior stability and high capacity of restacked molybdenum disulfide as anode material for lithium ion batteries. *Chem. Commun.* **46**, 1106-1108 (2010).
12. Cheng, L. *et al.* PEGylated WS_2 nanosheets as a multifunctional theranostic agent for in vivo dual-modal CT/photoacoustic imaging guided photothermal therapy. *Adv. Mater.* **26**, 1886-1893 (2014).
13. Chen, Y., Tan, C. L., Zhang, H. & Wang, L. Z. Two-dimensional graphene analogues for biomedical applications. *Chem. Soc. Rev.* **44**, 2681-2701 (2015).
14. Dumcenco, D. O., Kobayashi, H., Liu, Z., Huang, Y. S. & Suenaga, K. Visualization and quantification of transition metal atomic mixing in $Mo_{1-x}W_xS_2$ single layers. *Nat. Commun.* **4**, 1351 (2013).

15. Chen, Y. F. *et al.* Tunable band gap photoluminescence from atomically thin transition-metal dichalcogenide alloys. *ACS Nano* **7**, 4610-4616 (2013).
16. Gong, Y. J. *et al.* Band gap engineering and layer-by-layer mapping of selenium-doped molybdenum disulfide. *Nano Lett.* **14**, 442-449 (2014).
17. Li, H. L. *et al.* Growth of alloy $MoS_{2x}Se_{2(1-x)}$ nanosheets with fully tunable chemical compositions and optical properties. *J. Am. Chem. Soc.* **136**, 3756-3759 (2014).
18. Mann, J. *et al.* 2-Dimensional transition metal dichalcogenides with tunable direct band gaps: $MoS_{2(1-x)}Se_{2x}$ monolayers. *Adv. Mater.* **26**, 1399-1404 (2014).
19. Feng, Q. L. *et al.* Growth of large-area 2D $MoS_{2(1-x)}Se_{2x}$ semiconductor alloys. *Adv. Mater.* **26**, 2648-2653 (2014).
20. Kiran, V. *et al*. Active guests in the $MoS_2/MoSe_2$ host lattice: efficient hydrogen evolution using few-layer alloys of $MoS_{2(1-x)}Se_{2x}$. *Nanoscale* **6**, 12856-12863 (2014).
21. Funaki, K. *et al.* Liquid-phase exfoliation of ultrathin layered transition metal dichalcogenide nanosheets composed of solid-solution $Mo_{1-x}W_xS_2$. *Phys. Status Solidi A* **211**, 901-904 (2014).
22. Gong, Q. F. *et al.* Ultrathin $MoS_{2(1–x)}Se_{2x}$ alloy nanoflakes for electrocatalytic hydrogen evolution reaction. *ACS Catal.* **5**, 2213-2219 (2015).
23. Voiry, D., Mohite, A. & Chhowalla, M, Phase engineering of transition metal dichalcogenides. *Chem. Soc. Rev.* **44**, 2702-2712 (2015).
24. Voiry, D. *et al.* Enhanced catalytic activity in strained chemically exfoliated WS_2 nanosheets for hydrogen evolution. *Nat. Mater.* **12**, 850-855 (2013).
25. Voiry, D. *et al.* Conducting MoS_2 nanosheets as catalysts for hydrogen evolution reaction. *Nano Lett.* **13**, 6222-6227 (2013).
26. Lukowski, M. A. *et al.* Enhanced hydrogen evolution catalysis from chemically exfoliated metallic MoS_2 nanosheets. *J. Am. Chem. Soc.* **135**, 10274-10277 (2013).
27. Acerce, M., Voiry, D. & Chhowalla, M. Metallic 1T phase MoS_2 nanosheets as supercapacitor electrode materials. *Nat. Nanotechnol.* **10**, 313-318 (2015).
28. Kappera, R. *et al.* Phase-engineered low-resistance contacts for ultrathin MoS_2 transistors. *Nat. Mater.* **13**, 1128-1134 (2014).
29. Cho, S. *et al.* Phase patterning for ohmic homojunction contact in $MoTe_2$. *Science* **349**, 625-628 (2015).

30. Eda, G. *et al.* Photoluminescence from chemically exfoliated MoS_2. *Nano Lett.* **11**, 5111-5116 (2011).
31. Lin, Y.-C., Dumcenco, D. O., Huang, Y.-S. & Suenaga, K. Atomic mechanism of the semiconducting-to-metallic phase transition in single-layered MoS_2. *Nat. Nanotechnol.* **9**, 391-396 (2014).
32. Yu, Y. *et al.* Gate-tunable phase transitions in thin flakes of 1T-TaS_2. *Nat. Nanotechnol.* **10**, 270-276 (2015).
33. Mahler, B., Hoepfner, V., Liao, K. & Ozin, G. A. Colloidal synthesis of 1T-WS_2 and 2H-WS_2 nanosheets: applications for photocatalytic hydrogen evolution. *J. Am. Chem. Soc.* **136**, 14121-14127 (2014).
34. Zeng, Z. Y. *et al.* Single-layer semiconducting nanosheets: high-yield preparation and device fabrication. *Angew. Chem. Int. Ed.* **50**, 11093-11097 (2011).
35. Baker, M. A., Gilmore, R., Lenardi, C. & Gissler, W. XPS investigation of preferential sputtering of S from MoS_2 and determination of MoS_x stoichiometry from Mo and S peak positions. *Appl. Surf. Sci.* **150**, 255-262 (1999).
36. Mallouky, A. & Bernede, J. C. Characterization of $MoSe_2$ thin films. *Thin Solid Films* **158**, 285-298 (1988).
37. Su, S. H. *et al.* Band gap-tunable molybdenum sulfide selenide monolayer alloy. *Small* **10**, 2589-2594 (2014).
38. Chen, Y. F. *et al.* Composition-dependent Raman modes of $Mo_{1-x}W_xS_2$ monolayer alloys. *Nanoscale* **6**, 2833-2839 (2014).
39. Huang, X. *et al.* Solution-phase epitaxial growth of noble metal nanostructures on dispersible single-layer molybdenum disulfide nanosheets. *Nat. Commun.* **4**, 1444 (2013).
40. Py, M. A. & Haering, R. R. Structural destabilization induced by lithium intercalation in MoS_2 and related compounds. *Can. J. Phys.* **61**, 76-84 (1983).
41. Wang, H. *et al.* Electrochemical tuning of vertically aligned MoS_2 nanofilms and its application in improving hydrogen evolution reaction. *P. Natl. Acad. Sci. USA* **110**, 19701-19706 (2013).
42. Wu, M. X. *et al.* Economical and effective sulfide catalysts for dye-sensitized solar cells as counter electrodes. *Phys. Chem. Chem. Phys.* **13**, 19298-19301 (2011).

43. Chen, H. J. *et al.* In situ growth of a $MoSe_2$/Mo counter electrode for high efficiency dye-sensitized solar cells. *Chem. Commun.* **50**, 4475-4477 (2014).

44. O'regan, B. & Grätzel, M. A low-cost, high-efficiency solar cell based on dye-sensitized colloidal TiO_2 films. *Nature* **353**, 737-740 (1991).

45. Sun, H. *et al.* In situ preparation of a flexible polyaniline/carbon composite counter electrode and its application in dye-sensitized solar cells. *J. Phys. Chem. C* **114**, 11673-11679 (2010).

46. Wu, M., Lin, X., Hagfeldt, A. & Ma, T. Low-cost molybdenum carbide and tungsten carbide counter electrodes for dye-sensitized solar cells. *Angew. Chem. Int. Ed.* **50**, 3520-3524 (2011).

47. Koide, N., Islam, A., Chiba, Y. & Han, L. Improvement of efficiency of dye-sensitized solar cells based on analysis of equivalent circuit. *J. Photoch. Photobiol. A* **182**, 296-305 (2006).

48. Ren, X. *et al.* Se-doped MoS_2 nanosheet for improved hydrogen evolution reaction. *Chem. Commun.* DOI: 10.1039/C5CC06847A (2015).

49. Ho, C. H., Wu, C. S., Huang, Y. S., Liao, P. C. & Tiong, K. K. Temperature dependence of energies and broadening parameters of the band-edge excitons of $Mo_XW_{1-x}S_2$ single crystals. *J. Phys.: Condens. Matter* **10**, 9317-9328 (1998).

50. Ito, S. *et al.* Fabrication of thin film dye sensitized solar cells with solar to electric power conversion efficiency over 10%. *Thin Solid Films* **516**, 4613-4619 (2008).

Figures

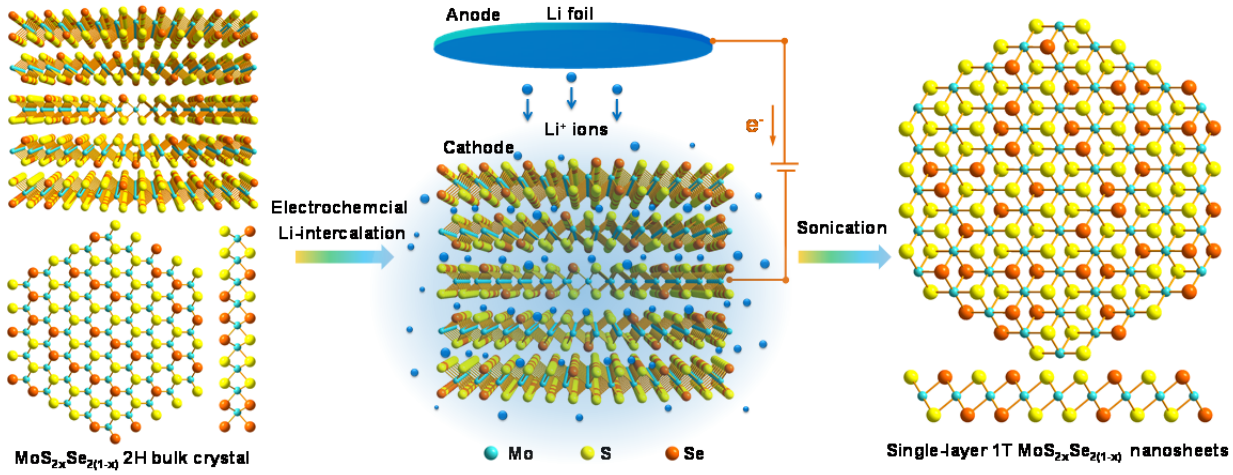

Scheme 1. Schematic illustration of preparation of single-layer ternary TMD nanosheets with high-concentration metallic 1T phase from their 2H-phase layered bulk crystals by using the electrochemical Li-intercalation and exfoliation method. Note that $MoS_{2x}Se_{2(1-x)}$ is used as an example in this scheme.

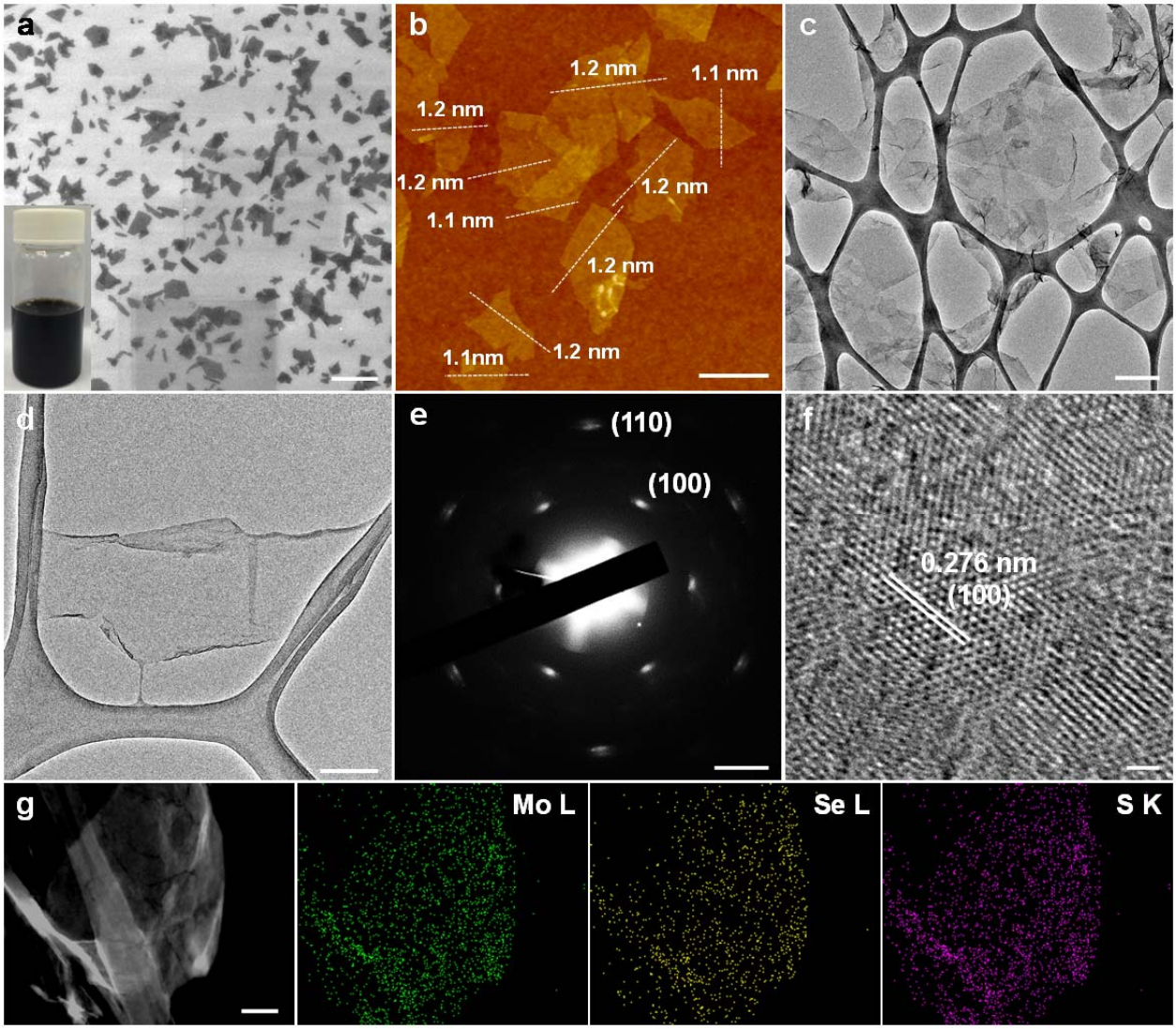

Figure 1. Characterization of $MoS_{2x}Se_{2(1-x)}$ nanosheets. (a) SEM image and (b) AFM height image of $MoS_{2x}Se_{2(1-x)}$ nanosheets (scale bars, a: 2 μm; b: 500 nm). Inset in (a): Photograph of colloidal suspension of $MoS_{2x}Se_{2(1-x)}$ nanosheets. (c) TEM image of $MoS_{2x}Se_{2(1-x)}$ nanosheets (scale bar, 500 nm). (d) TEM image of a typical $MoS_{2x}Se_{2(1-x)}$ nanosheet (scale bar, 200 nm). (e) The corresponding SAED pattern of the $MoS_{2x}Se_{2(1-x)}$ nanosheet in (d) (scale bar, 2 1/nm). (f) HRTEM image of a typical $MoS_{2x}Se_{2(1-x)}$ nanosheet (scale bar, 1 nm). (g) EDS elemental mapping of a typical $MoS_{2x}Se_{2(1-x)}$ nanosheet (scale bar, 100 nm).

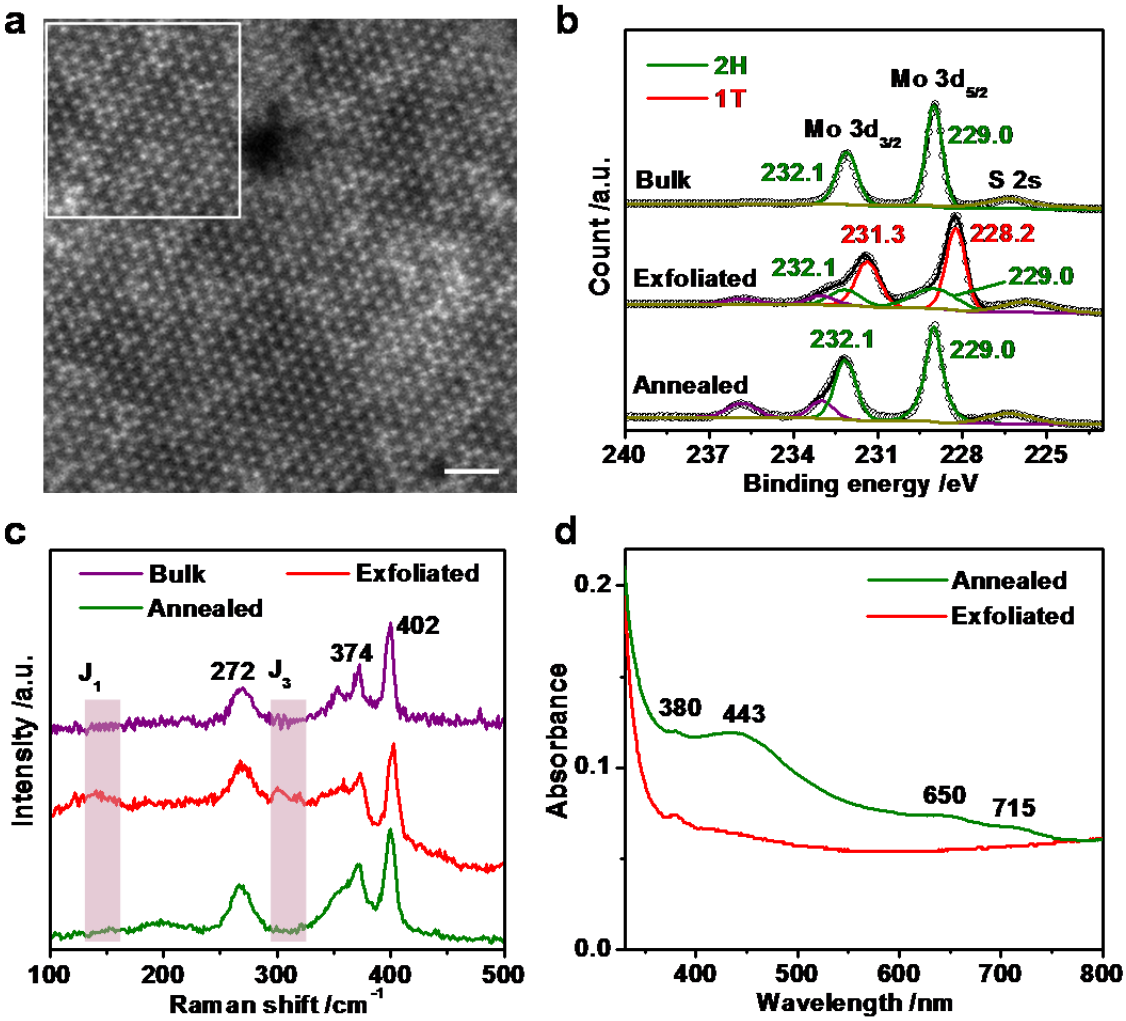

Figure 2. Characterization of the presence of 1T phase in the exfoliated $MoS_{2x}Se_{2(1-x)}$ nanosheets. (a) Atomic STEM image of a typical exfoliated $MoS_{2x}Se_{2(1-x)}$ nanosheet (scale bar, 1 nm). Supplementary Figure 5 gives individual Mo (light blue dot) and Se (orange dot) atoms in the white squire in (a). (b) High-resolution XPS Mo 3d spectrum of bulk crystal of $MoS_{2x}Se_{2(1-x)}$, and the exfoliated and annealed $MoS_{2x}Se_{2(1-x)}$ nanosheets. (c) Raman spectra of bulk crystal of $MoS_{2x}Se_{2(1-x)}$, and the exfoliated and annealed $MoS_{2x}Se_{2(1-x)}$ nanosheets. (d) UV-vis spectra of exfoliated and annealed $MoS_{2x}Se_{2(1-x)}$ nanosheet films on glass.

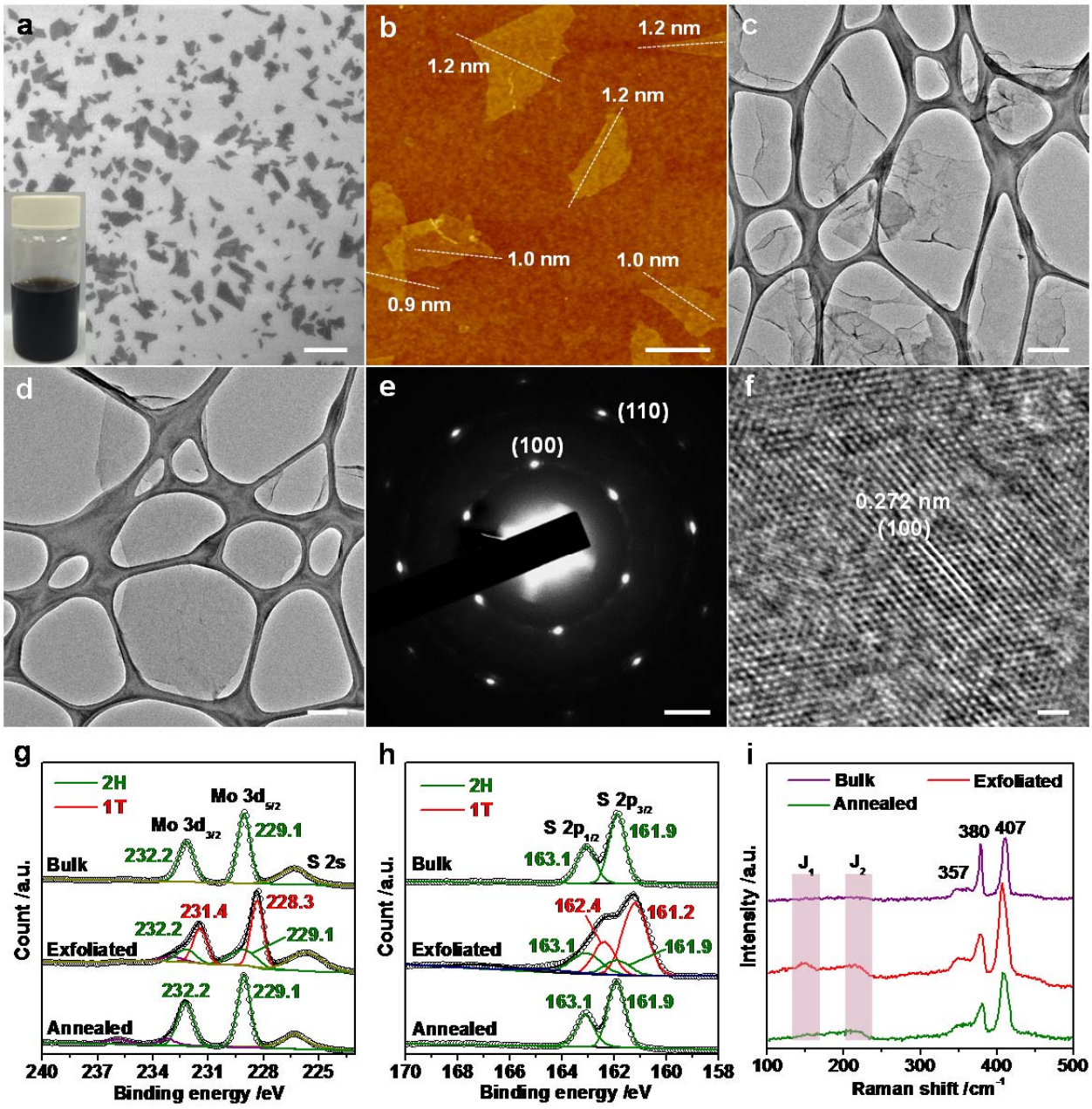

Figure 3. Characterization of $Mo_xW_{1-x}S_2$ nanosheets. (a) SEM image and (b) AFM height image of $Mo_xW_{1-x}S_2$ nanosheets (scale bars, a: 2 μm; b: 500 nm). Inset in (a): Photograph of the colloidal suspension of $Mo_xW_{1-x}S_2$ nanosheets. (c) TEM image of $Mo_xW_{1-x}S_2$ nanosheets (scale bar, 500 nm). (d) TEM image of a typical $Mo_xW_{1-x}S_2$ nanosheet (scale bar, 400 nm). (e) The corresponding SAED pattern of the $Mo_xW_{1-x}S_2$ nanosheet in (d) (scale bar, 2 1/nm). (f) HRTEM image of a typical $Mo_xW_{1-x}S_2$ nanosheet (scale bar, 1 nm). (g) High-resolution Mo 3d XPS spectra of bulk crystal of $Mo_xW_{1-x}S_2$, and the exfoliated and annealed $Mo_xW_{1-x}S_2$ nanosheets. (h) High-resolution S 2p XPS spectra of bulk crystal of $Mo_xW_{1-x}S_2$, and the exfoliated and annealed

$Mo_xW_{1-x}S_2$ nanosheets. (i) Raman spectra of bulk crystal of $Mo_xW_{1-x}S_2$, and the exfoliated and annealed $Mo_xW_{1-x}S_2$ nanosheets.

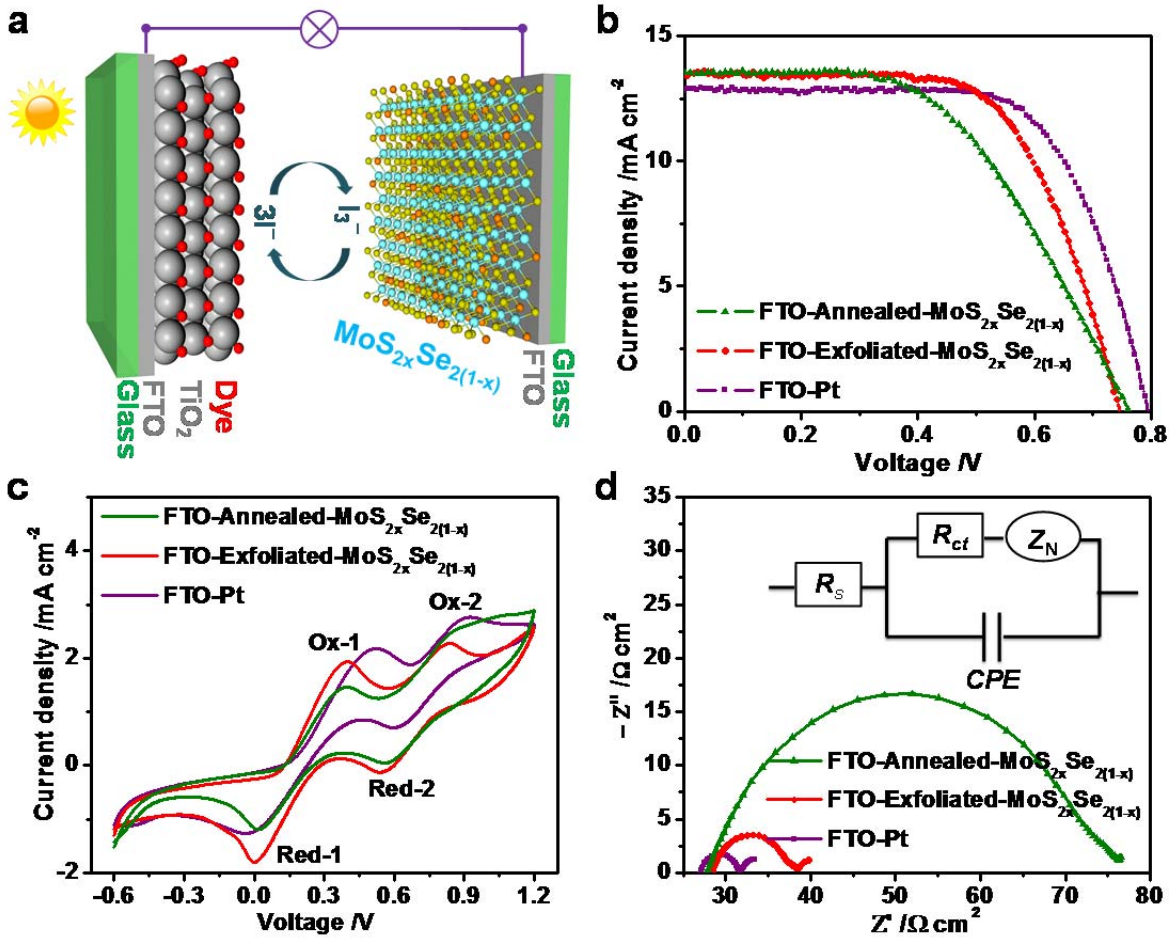

Figure 4. DSSCs based on $MoS_{2x}Se_{2(1-x)}$ nanosheets. (a) Schematic illustration of a typical assembled DSSC with N719 dye-sensitized TiO_2 photoanode and FTO-Exfoliated-$MoS_{2x}Se_{2(1-x)}$ CEs. (b) *J-V* curves of DSSCs with FTO-Exfoliated-$MoS_{2x}Se_{2(1-x)}$, FTO-Annealed-$MoS_{2x}Se_{2(1-x)}$ and FTO-Pt used as CEs measured under simulated sunlight 100 mW cm^{-2} (AM 1.5). (c) CV curves of FTO-Exfoliated-$MoS_{2x}Se_{2(1-x)}$, FTO-Annealed-$MoS_{2x}Se_{2(1-x)}$ and FTO-Pt CEs in the acetonitrile solution containing 10 mM of LiI, 1 mM of I_2, and 0.1 M of $LiClO_4$ (supporting electrolyte). (d) Nyquist plots of a symmetric dummy cell with configuration of two identical FTO-Exfoliated-$MoS_{2x}Se_{2(1-x)}$, FTO-Annealed-$MoS_{2x}Se_{2(1-x)}$ or FTO-Pt electrodes (inset: a fitting equivalent circuit).

Table 1. Photovoltaic parameters of DSSCs with different counter electrodes and simulated data from the fitted EIS curves.

Counter electrode	V_{oc} (V)	J_{sc} (mA cm^{-2})	*FF* (%)	PCE (%)	R_s (Ω cm^2)	R_{ct} (Ω cm^2)
FTO-Pt	0.80	12.82	0.69	7.0	27.07	2.28
FTO-Exfoliated-$MoS_{2x}Se_{2(1-x)}$	0.75	13.40	0.65	6.5	28.40	4.60
FTO-Annealed-$MoS_{2x}Se_{2(1-x)}$	0.76	13.52	0.52	5.4	27.92	23.25